ICCFD13-2026-188

One-side and ghost-cell immersed boundary methods for hypersonic flows simulation

D. Ninni*, F. Bonelli* and G. Pascazio*
Corresponding author: davide.ninni@poliba.it
* Department of Mechanics, Mathematics and Management, Polytechnic University of Bari, Via Re David 200, Bari, Italy

Abstract: The use of *immersed-boundary* (IB) technique represents a valuable alternative in the context of hypersonic flow simulations. Indeed, due to the strong meshing effort and/or the difficoulty in re-meshing the fluid domain in the case of an ablated surface, classical *body-fitted* (BF) approaches require the use of unstructured or multi-block grids, leading to a more complex data structure to handle in the numerical solver. This work presents numerical results for hypersonic flows obtained with two different IB techniques, compared to reference results obtained with the corresponding BF solver.

Keywords: Immersed Boundary, Hypersonics, Thermochemical non-equilibrium, GPU.

1. Introduction

Numerical simulations of hypersonic flows are challenging due to the combination of thermophysical modeling and numerical strategy. Specifically, in the context of atmospheric vehicle entry, the solver has to deal with strong shock waves which provoke energy excitation and molecular dissociation [1]. This leads to a tremendous heat transfer on the vehicle surface, mainly due to conduction. However, in the presence of gas-surface interactions, mass diffusion becomes a relevant contribution to the total heat flux due to catalysis and ablation [2], the latter rising from the interaction between the chemical species in the boundary layer and the material composing the Thermal Protection System (TPS). Nitridation and/or oxidation processes may take place, pushing the gas far from the wall (*blowing effect*) [3] and mitigating the heat flux on the surface by material decomposition and mass loss. In some cases, the surface recesses with a finite velocity, provoking a shape change of the TPS.

Most of the numerical solvers [4, 5] in the scientific community employ *body-fitted* (BF) grids, which allow the use of large cell aspect ratios, thus ensuring very high wall normal resolution in the boundary layer. However, when dealing with complex/moving geometries, multiblock structured grids or unstructured grids are necessary. As an alternative, *immersed-boundary* (IB) techniques [6, 7] exploit Cartesian meshes for the fluid domain, where the geometry is embedded as a Lagrangian (solid) domain, as illustrated in Fig. 1. The governing equations are then solved in the Eulerian (fluid) domain with a forcing term which accounts for the forces exchanged between the fluid and the body, such that the equations obey the desired boundary condition on the surface (e.g., no-slip). Of course, numerical solution of the governing equations is not needed within the solid. Hence, a ray-tracing procedure is used to identify all the cells whose center lies into the body (*solid cells*). Once these are identified, the fluid cells having at least one neighbor in the solid domain are tagged as *interface cells* cells (yellow squares in the right side of Fig. 1): in these cells, an appropriate reconstruction of the flow field variables is needed to satisfy the wall boundary condition. In some cases, the identification of *interface-solid cells* (or simply *ghost cells*) is needed to impose a proper boundary condition on the wall. These cells are the solid cells having at least one neighbor in the fluid domain, as shown in Fig. 2(b).

This paper is organized as follows: the numerical solver is described in Sec. 2, which provides details about the IB methods implemented; a brief description of the thermophysical modeling is provided in Sec. 3. Discussion about numerical results is presented in Sec. 4.

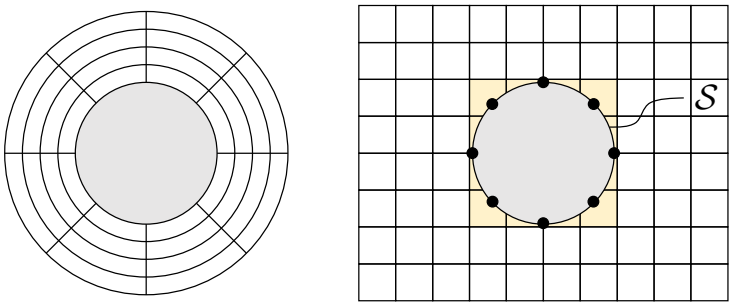

Figure 1: Comparison of *body-fitted* (left) and *immersed boundary* (right) meshes.

2. Numerical approach

2.1 Governing equations

The original BF solver (Damiso) is developed in a Finite-Volume approach, within an MPI-CUDA framework for multi-GPU executions [8]. The integral form of the 2D equations is

$$\int_{\Omega_0} \frac{\partial}{\partial t}\mathbf{U} d\Omega + \oint_{S_0} \mathbf{F}\cdot\mathbf{n} dS = \int_{\Omega_0} \mathbf{W} d\Omega \tag{1}$$

being S_0 the whole surface defining the control volume Ω_0, whereas $\mathbf{U}$, $\mathbf{F}$ and $\mathbf{W}$ represent the vectors of conservative variables, fluxes and source terms, respectively:

$$\mathbf{U} = \begin{bmatrix} \rho_1 \\ \vdots \\ \rho_{N_s} \\ \rho\, u \\ \rho\, v \\ \rho\, E \\ \rho\varepsilon_{ve} \end{bmatrix} \tag{2a}$$

$$\mathbf{F} = \left(\mathbf{F}_I^x - \mathbf{F}_V^x, \mathbf{F}_I^y - \mathbf{F}_V^y\right) \tag{2b}$$

$$\left(\mathbf{F}_I^x, \mathbf{F}_I^y, \mathbf{F}_I^z\right) = \begin{bmatrix} \rho_1\mathbf{u} \\ \vdots \\ \rho_{N_s}\mathbf{u} \\ \rho\mathbf{u}\otimes\mathbf{u} + p\overline{\overline{\mathrm{I}}} \\ (\rho\, E + p)\mathbf{u} \\ \rho\varepsilon_{ve}\mathbf{u} \end{bmatrix} \qquad \left(\mathbf{F}_V^x, \mathbf{F}_V^y\right) = \begin{bmatrix} -\rho_1\boldsymbol{\mathcal{V}}_1 \\ \vdots \\ -\rho_{N_s}\boldsymbol{\mathcal{V}}_{N_s} \\ \overline{\overline{\sigma}} \\ \mathbf{u}\cdot\overline{\overline{\sigma}} - \mathbf{q} \\ -\mathbf{q}_{ve} \end{bmatrix} \tag{2c}$$

$$\mathbf{W} = \begin{bmatrix} \dot{\omega}_1 \\ \vdots \\ \dot{\omega}_{N_s} \\ 0 \\ 0 \\ 0 \\ \dot{\omega}_{ve} \end{bmatrix} \tag{2d}$$

In the above expressions, ρ is the mixture density, p the thermodynamic pressure, E the total specific energy and $\mathbf{u} = (u, v)$ the velocity vector and its components in the Cartesian reference. A continuity equation is solved for each species, so that $\rho = \sum_s^{N_s} \rho_s$ being N_s the total number of species. The other quantities in the viscous flux vector are the species diffusion velocities ($\boldsymbol{\mathcal{V}}_s$), the stress tensor ($\overline{\overline{\sigma}}$) and the heat flux appearing in its total ($\mathbf{q}$) and vibro-electronic ($\mathbf{q}_{ve}$) contributions. These read:

$$\rho_s \boldsymbol{\mathcal{V}}_s = -\rho \mathcal{D}_s \nabla Y_s + \rho \mathbf{V}_c \tag{3}$$

$$\overline{\overline{\sigma}} = \mu \left[\nabla \mathbf{u} + (\nabla \mathbf{u})^T \right] - \frac{2}{3} \mu \left(\nabla \cdot \mathbf{u} \right) \bar{\bar{\mathrm{I}}} \tag{4}$$

$$\mathbf{q} = -\lambda_{tr} \nabla T - \lambda_{ve} \nabla T_{ve} + \sum_{s=1}^{N_s} \rho_s h_s \boldsymbol{\mathcal{V}}_s \tag{5}$$

$$\mathbf{q}_{ve} = -\lambda_{ve} \nabla T_{ve} + \sum_{s=1}^{N_s} \rho_s \varepsilon_{ve,s} \boldsymbol{\mathcal{V}}_s \tag{6}$$

Eq. (3) is the Fick law to account for mass diffusion phenomenon. In such expression, $\mathbf{V}_c = \sum_s \mathcal{D}_s \nabla Y_s$ is a correction term to ensure mass conservation [9]. The total heat flux is composed of three contributions, which are the translational (conductive), vibro-electronic and diffusive parts, the latter including the total specific enthalpy of each pseudo-species (h_s). Transport properties, namely the mixture viscosity (μ), thermal conductivity (λ_{tr}), vibro-electronic thermal conductivity (λ_{ve}) and species diffusion coefficient ($\mathcal{D}_s$) are calculated by means of mixing rules [10, 11, 12, 13], starting from accurate viscosity-type collision integrals evaluation for single-species properties [14]. The source terms due to chemical non-equilibrium ($\dot{\omega}_s$) and thermal non-equilibrium ($\dot{\omega}_{ve}$) are presented in section 3.1.

Inviscid fluxes are discretized using the Steger-Warming flux vector splitting [15], combined with a second-order accurate MUSCL reconstruction [16] and *minmod* limiter function. Interface gradients for diffusive terms are reconstructed with a centered, second-order accurate scheme. Time integration is split in two steps: since the code is written in an MPI-CUDA environment to exploit GPU capabilities [2], an explicit third-order accurate Runge-Kutta scheme [17] is used to advance conservative flow variables, thus solving homogeneous equations; in the second step, an implicit, iterative Gauss-Seidel scheme [18] is used to update thermochemical mixture properties, allowing for reasonable time-step sizes and avoiding numerical instability.

2.2 Immersed Boundary forcing

Immersed boundary forcing is used to apply a proper wall boundary condition. Two different techniques are employed in this work. The first one is based on a one-side forcing term (IB-1) which follows the idea proposed by Balaras [19], who extended the 1D reconstruction previously introduced by Fadlun [20]. By means of a ray-tracing procedure, the cells of the Eulerian domain are tagged as *solid*, *interface* or *fluid* (see Fig. 2(a)). The first ones lie within the Lagrangian surface, whereas the *interface* cells are defined have at least one neighbor in the solid domain. The numerical solution near the wall can be linearly reconstructed interpolating the values in the surrounding cells of the *interfaces*, as shown in Fig. 2(a). Cell I is projected on the wall (point W) along the normal direction. A support domain is then found in the nearest cells, namely cells A and B, so that:

$$\phi_{\mathrm{I}} = C_1 x_{\mathrm{I}} + C_2 y_{\mathrm{I}} + C_3 \tag{7}$$

where coefficients C_1, C_2 and C_3 are computed applying the same formula in points A, B and W. The

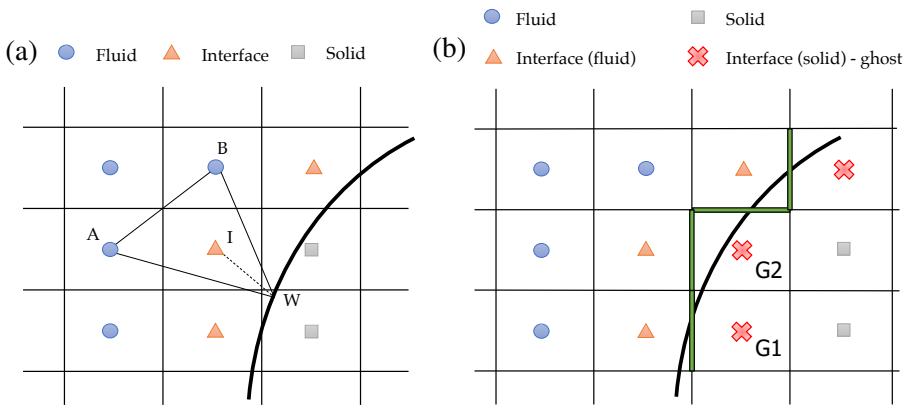

Figure 2: Tagging of the IB-1 (a) and IB-2 (b) methods.

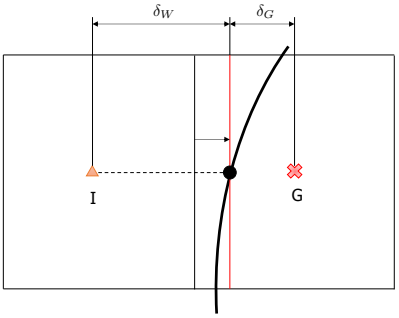

Figure 3: Sketch of the extrapolation stencil for IB-2 method.

extension to Neumann boundary condition is straightforward. Moreover, in this formulation the *solid* cells do not play a key role, since the numerical solution in the *interface* cells is not a function of that in the *solid* cells. Conventionally, the wall temperature (for isothermal walls) and null velocity are imposed in the *solid* cells. However, this approach is locally non-conservative since the governing equations are not actually solved at *interface* cells. In order to overcome this drawback, it is affordable to develop a ghost-cell based method (IB-2). The ghost cells are referred to as *interface solid* cells, and they are defined as the *solid* cells having at least one neighbor in the fluid domain (see Fig 2(b)). The philosophy of this method is to apply the same flux formulation also on the faces near the wall (green surfaces in Fig. 2(b)). In this formulation, a reconstruction of the numerical solution is needed in the ghost cells, where the value of the flow variables is extrapolated from the fluid domain so as to impose boundary conditions. Following the notation in Fig. 3, the solution in the ghost cell is evaluated as

$$\phi_G = \phi_W - \frac{\delta_G}{\delta_W}\left(\phi_\mathrm{I} - \phi_W\right) \tag{8}$$

so allowing for a locally conservative flux formulation in a finite-volume framework.

3. Thermophysical modeling

3.1 Kinetic model

Dealing with hypersonic entry flows, a thermophysical model is needed to account for non-equilibrium phenomena. For this purpose, the well-known multitemperature Park model [21] is employed. Reaction rate are taken from references in the literature for neutral air mixture [22] and contaminated air mixture [23]. In Eq. (2d) the source term $\dot{\omega}_s$ indicates the production/loss term of species s due to kinetic processes. Its expression is given by the law of mass action

$$\dot{\omega}_s = \mathcal{M}_s \sum_{r=1}^{N_r} a_{s,r} \left(k_{f,r} \prod_{s=1}^{N_s} c_s^{|a'_{s,r}|} - k_{b,r} \prod_{s=1}^{N_s} c_s^{|a''_{s,r}|} \right) \tag{9}$$

where N_r is the total number of reactions, $\mathcal{M}_s$ and c_s indicate the molecular weight and concentration of species s, respectively, whereas $a'_{s,r}$ and $a''_{s,r}$ are the stoichiometric coefficients of species s in reaction r when the species is a reactant ($'$, negative) or a product ($''$, positive). Indeed, it holds $a_{s,r} = |a''_{s,r}| - |a'_{s,r}|$. Concerning the vibro-electronic energy transport equation, $\dot{\omega}_{ve}$ represents gain/dissipation of vibro-electronic energy due to chemistry and energy transfer mechanisms

$$\dot{\omega}_{ve} = \dot{\omega}_{CV} + \dot{\omega}_{CE} + \dot{\omega}_{VT} \tag{10}$$

where $\dot{\omega}_{CV}$ and $\dot{\omega}_{CE}$ represent the chemistry-vibration and chemistry-electronic coupling, responsible for the rate of change of vibrational and electronic energy due to chemical processes; these are modeled through a non-preferential approach [24] for which each internal state has the same probability to dissociate, namely:

$$\dot{\omega}_{CV} = \sum_s \dot{\omega}_s e_{vib} \qquad \dot{\omega}_{CE} = \sum_s \dot{\omega}_s e_{el} \tag{11}$$

where $\dot{\omega}_s$ is the chemical source term coming from the law of mass action in Eq. (9). Vibrational-translational relaxation source term, $\dot{\omega}_{VT}$, is modeled through the Landau-Teller formulation

$$\dot{\omega}_{VT} = \sum_s \rho_s \frac{e_{vib,s}(T) - e_{vib,s}(T_{vib})}{\tau_s} \tag{12}$$

being τ_s the relaxation time evaluated through the Millikan-White expression [21, 22, 25].

3.2 Gas-Surface Interation modeling

In the case of gas-surface interaction (GSI) processes like catalysis or ablation, a surface mass balance is solved to calculate the chemical composition at wall. With the assumption of a steady-state ablation boundary condition, the mass balance reads:

$$\left(\boldsymbol{j}_{s,wall} + \rho_{s,wall} \boldsymbol{u}_{blow} \right) \cdot \boldsymbol{n} = \dot{\omega}_{surf,s} \tag{13}$$

where $\boldsymbol{u}_{blow}$ represents the gas velocity coming from the surface due to *mass-blowing* effect and $\dot{\omega}_{surf,s} = \dot{\omega}_{cata,s} + \dot{\omega}_{abla,s}$ is the source terms due the surfece kinetics (i.e. catalysis and/or ablation). Summing over all the species, diffusion terms and catalysis source terms are null by construction and the massblowing rate can be defined as:

$$(\rho_{wall} \boldsymbol{u}_{blow}) \cdot \boldsymbol{n} = \sum_s \dot{\omega}_{abla,s} \longrightarrow \boldsymbol{u}_{blow} = \frac{\dot{m}_{blow}}{\rho_{wall}} \tag{14}$$

The modeling of catalysis and ablation follows a phenomenological approach for which a probability coefficient β_s is defined for each kinetic process. In this work, only heteronuclear catalysis is considered, so:

$$\mathrm{N} + \mathrm{N} \longrightarrow \mathrm{N_2} \qquad \mathrm{O} + \mathrm{O} \longrightarrow \mathrm{O_2}$$

for which the source terms is defined as

$$\dot{\omega}_{cata,a} = \beta_a m_a \mathcal{F}_{imp,a} \tag{15}$$

the subscript a referring to an atomic species with particle mass m_a. A similar source term is defined for the corresponding molecule m, so that $\dot{\omega}_{cata,m} = -\dot{\omega}_{cata,a}$. In the presence of an isothermal wall and an approximately Maxwellian internal states distribution, the impinging mass flux of a generic species s is given by [26]:

$$\mathcal{F}_{imp,s} = n_s \sqrt{\frac{k_B T_w}{2\pi m_s}} \tag{16}$$

where k_B is the Boltzmann constant and T_w is the wall temperature. Specifically, $\beta_a = 1$ indicates a fully-catalytic wall. In the case of ablation, the source terms still needs the definition of a probability coefficient. In this work, the nitridation process s considered for a reference test-case

$$\mathrm{C}_s + \mathrm{N} \longrightarrow \mathrm{CN}$$

where subscript s stands for *surface*. This process has been widely investigated in the VKI Plasmatron facility [27] and the probability coefficient derived from the experiments

$$\beta_{\mathrm{CN}} = 0.0791 \exp(-5653/T_w) \tag{17}$$

turned out to be effective for a wide range of wall temperatures.

4. Numerical results

4.1 Supersonic perfect gas flow

Preliminary analysis is devoted to the investigation of a supersonic flow past a cylinder ($r = 0.05$ m), which is referred to as *M3C* test. The flow conditions are reported in Table 1. The wall is considered isothermal and non-catalytic. This test case is an essential starting point for the development of immersed boundary methods as the mixture is considered frozen and the thermal boundary layer is expected to be thick enough to reconstruct the temperature gradient while maintaining a reasonable resolution of the grid near the surface. Indeed, two different BF simulations have been performed to estimate a proper wall resolution of the grid. From the mesh independence analysis shown in Appendix A, grid converged heat flux is obtained for a wall resolution of $\Delta n_w = 1 \times 10^{-5}$ m.

Table 1: Free stream conditions for the *M3C* test.

M_∞	T_∞ [K]	p_∞ [Pa]	ρ_∞ [kg/m^3]	T_w [K]
3	293	7.43	8.77×10^{-5}	293

Stagnation line profiles are reported in Fig. 4 in terms of gas temperature and axial velocity. IB results are in an excellent agreement with BF prediction: shock location is correctly captured and the boundary layer well reproduced. However, observing the behaviour close to the stagnation point, IB-1 method predicts a velocity inversion, which is nonphysical. This is probably due to the interpolation method which does not ensure conservation since the solution in the interface cells is not provided by the integration of the governing equation but by the forcing term. On the contrary, governing equations are still solved in the

interface cells for the IB-2, thus providing a much more reliable result.

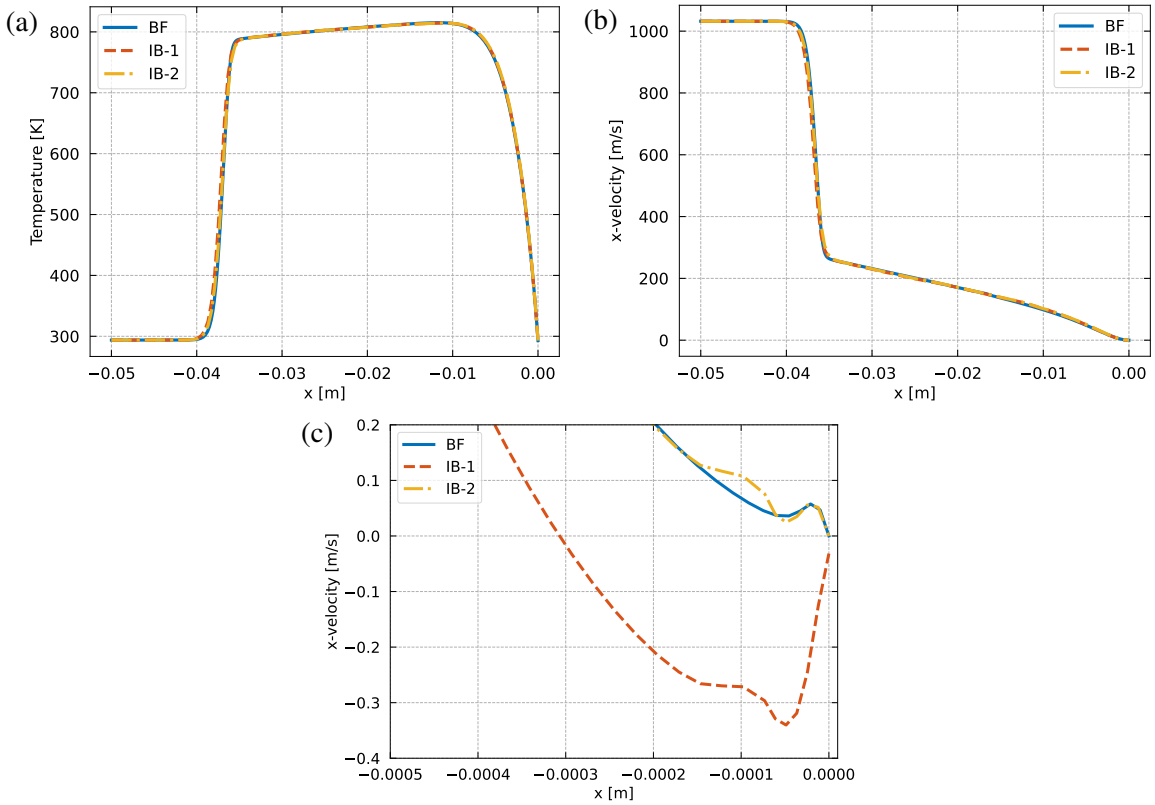

Figure 4: Temperature (a) and axial velocity (b) profiles along the stagnation streamline for the *M3C* test. Zoom of the velocity profile in the stagnation point (c).

Wall quantity profiles are shown in Fig. 5. Wall pressure reconstruction is in an excellent agreement with BF results. Such a result is expected because of the nature of the wall boundary condition on the static pressure: being a Neumann type, no gradient must be reconstructed in the boundary layer, thus permitting for a much easier numerical solution. Some discrepancies are observed for the wall shear stress and heat flux. Indeed, their reconstruction necessitates of gradient evaluation, which might be inaccurate in the case of low mesh resolution at wall. Nevertheless, comparison between IB and BF results is still in an acceptable agreement.

4.2 Hypersonic reactive flow

Results of the proposed IB techniques are presented also for the hypersonic flow past a cylinder [28] with a radius of $r = 0.045$ m. Table 2 summarizes the free stream conditions of the flow, giving also indications about the mixture composition in terms of species mass fractions. In the experimental campaign the wall was kept at constant temperature ($T_w = 300$ K). However, in order to put in evidence the relevance of the thermal wall boundary condition, both isothermal and adiabatic boundary conditions have been investigated. After a mesh independence study (shown in Appendix A) a BF grid with 400×200 cells and a wall normal resolution of 5×10^{-8} m has been selected as reference. Given the constraint on the cell aspect ratio for Cartesian grids, IB mesh can not achieve such a high wall resolution. Hence, the IB grid presents a wall normal resolution of 7×10^{-6} m (MeshI). However, assuming that this would lead to inaccurate wall gradients, one more effort has been done to build a alternative grid (MeshII). Hence, it has been coarsen on the shock and refined at wall ($\Delta n_w = 3 \times 10^{-6}$ m) while maintaining an approximately constant number of cells. Nevertheless, numerical results seem to be almost insensitive in terms of stagnation line profiles, which are shown only for MeshI. On the other hand, wall quantity profiles are shown for both IB meshes.

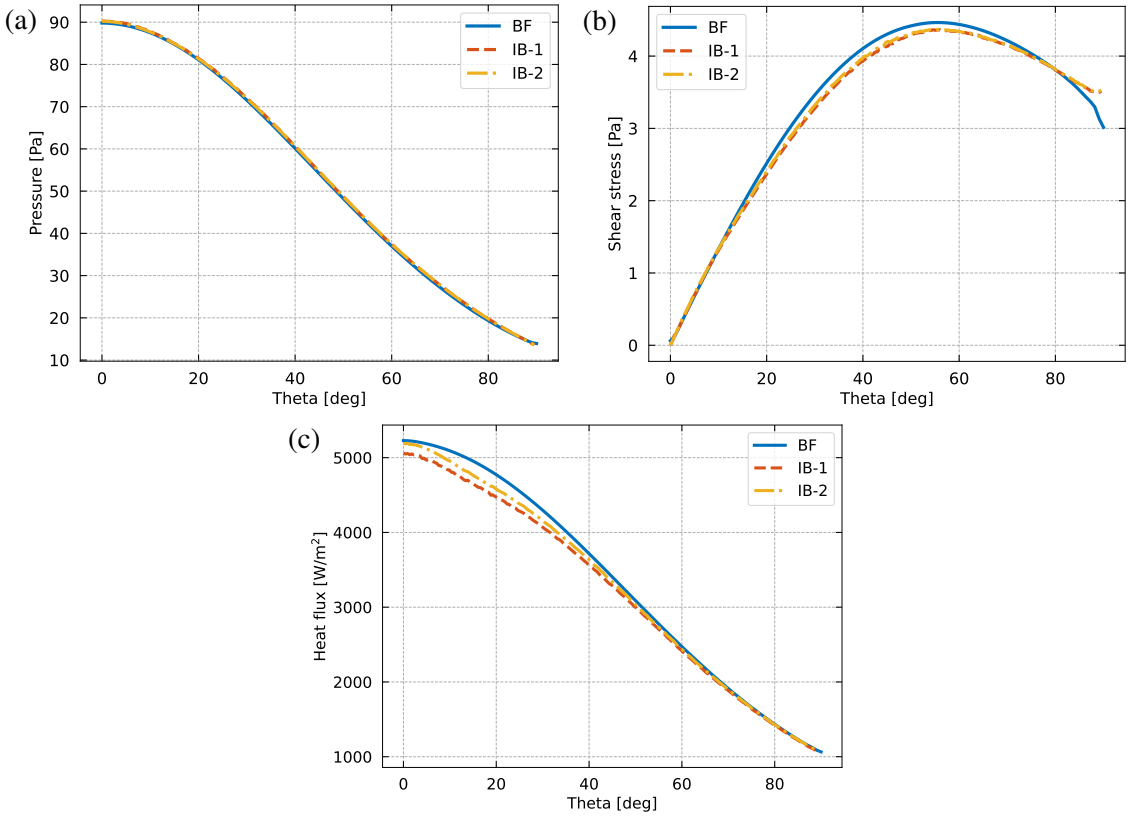

Figure 5: Pressure (a), shear stress (b) and heat flux (c) wall profiles for the *M3C* test.

Temperature and mass fraction profiles along the stagnation line are illustrated in Fig. 6. It is evident that the most critical issue is the reconstruction of the temperature near the wall: this is essential for an accurate reproduction of the thermal boundary layer, which influences the accuracy of the results in terms of shock stand-off distance. The large error (about 12%) of the IB-1 method with respect to the BF approach is mainly due to an nonphysical description of the thermal boundary layer. An inset of the stagnation point region is provided in Fig. 6(b): the concavity of the curve of the IB-1 method is completely different with respect to IB-2, which instead follows the BF result. An inaccurate evaluation of the temperature leads to inaccurate reaction speeds, provoking nonphysical kinetics. For this reason, mass fraction shown in Fig. 6(c) are not illustrated for IB-1 method.

Table 2: Free stream conditions for the *Knight* case [28].

M_∞	T_∞ [K]	p_∞ [Pa]	Y_{N_2}	Y_{O_2}	Y_{NO}	Y_N	Y_O
8.98	901	476	0.7543	0.00713	0.01026	6.5×10^{-7}	0.2283

It is worth to point out two relevant aspects of this test case, which make it different from the perfect gas test. First of all, the higher free stream Mach number regime, which is the main driving factor of the stronger shock wave and thinner boundary layer. Secondly, the non-negligible chemical non-equilibrium. Hence, on completion of the relevance of temperature reconstruction as main issue for the discrepancies observed in the numerical results, two additional tests are here proposed. The same simulation has been performed:

1. under the assumption of a perfect gas mixture while maintaining an isothermal wall;
2. under the assumption of a reactive gas mixture in the presence of an adiabatic wall.

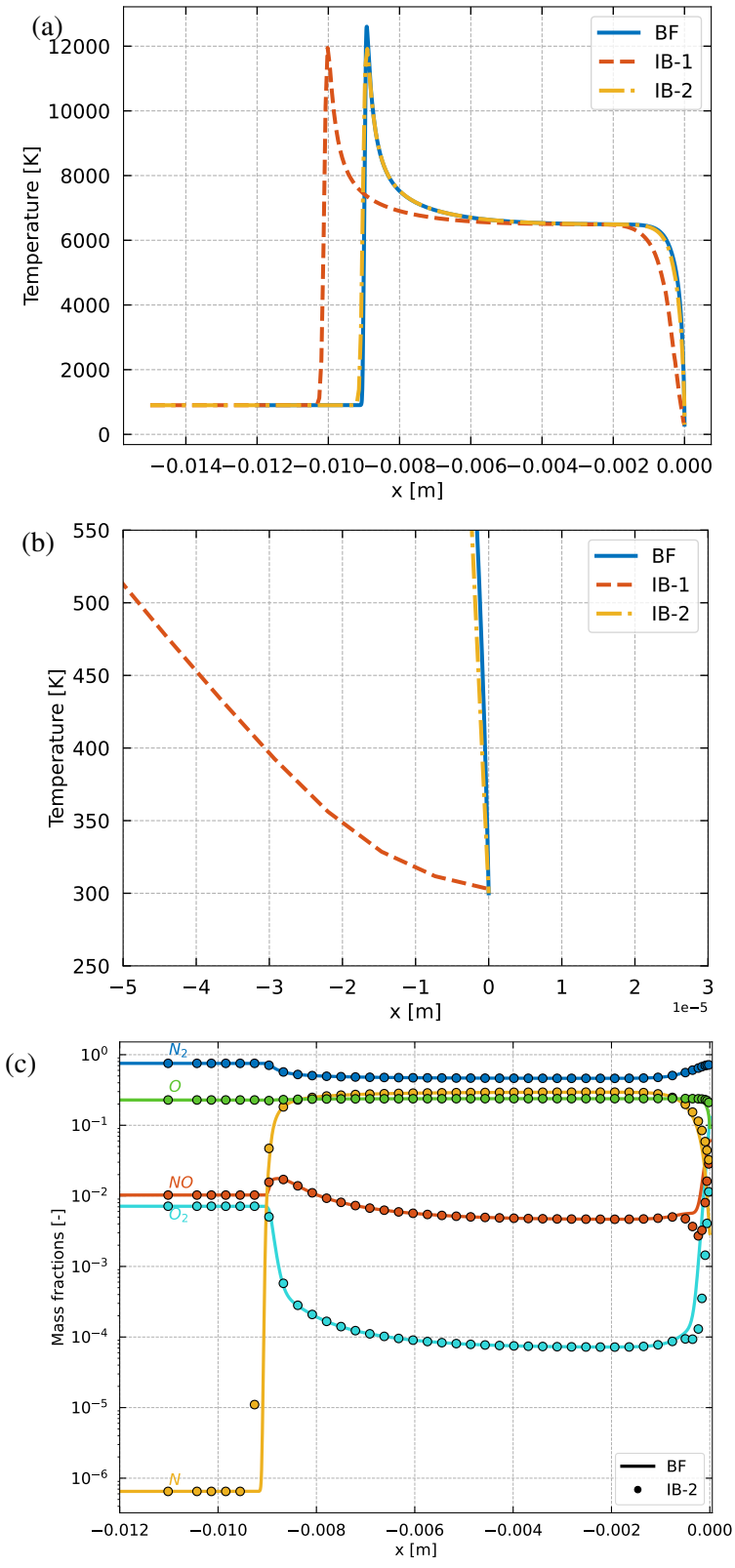

Figure 6: Temperature (a) and species mass fraction (c) profiles along the stagnation streamline for the isothermal *Knight* test (a). Zoom of temperature profile in the stagnation point (b).

Numerical results for this simulations are shown in Fig. 7.

The perfect gas test is not meant to be physically accurate, but its purpose is to isolate a specific issue

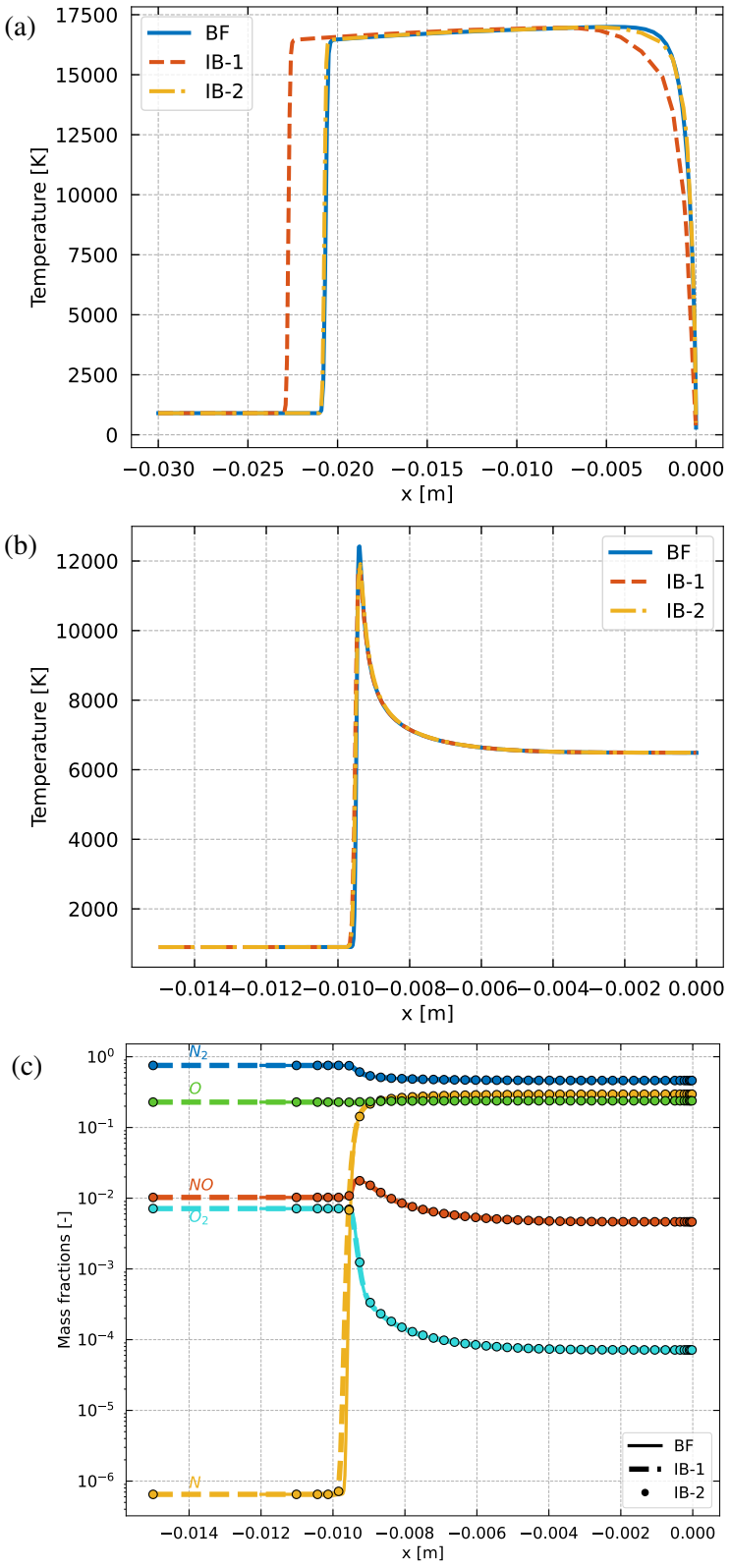

Figure 7: Temperature along the stagnation line for the *Knight* case under the assumption of perfect gas (a) and adiabatic wall (b). Species mass fraction profiles along the stagnation streamline for the adiabatic case (c).

of the simulation. As expected, the shock stand-off distance is much larger with respect to the reactive flow. Chemical reactions across the shock absorb most of the energy content due to dissociation, making

the shock wave locate much closer to the surface. As a consequence, also the peak temperature is larger. However, IB-2 is very accurate, providing a shock location in accordance with the BF approach. On the contrary, the same, aforementioned discrepancy with the IB-1 is here again observed. As a matter of fact, when an adiabatic wall is considered, both IB methods overlap to the BF profile, as shown in Fig. 7(b). A correct trend of the gas temperature is translated into a correct mass fraction estimation. Indeed, Fig. 7(c) reports an excellent agreement between IB and BF results in terms of gas composition. This analysis confirms that the main issue of IB methods, when applied in hypersonics, is the temperature reconstruction in the thermal boundary layer. It is worth specifying that the same conclusion may be drawn for the gas velocity, which also needs the evaluation of wall gradients. However, velocity gradient are not as sharper as the temperature one (i.e. the kinematic boundary layer is thicker than the thermal boundary layer) thus allowing for a smoother numerical solution even on coarser meshes.

Results for wall quantities are reported in Fig. 8. The first relevant observation is that the static pressure is well reconstructed in both IB simulations even on the coarser mesh, although IB1 slightly overestimates it.

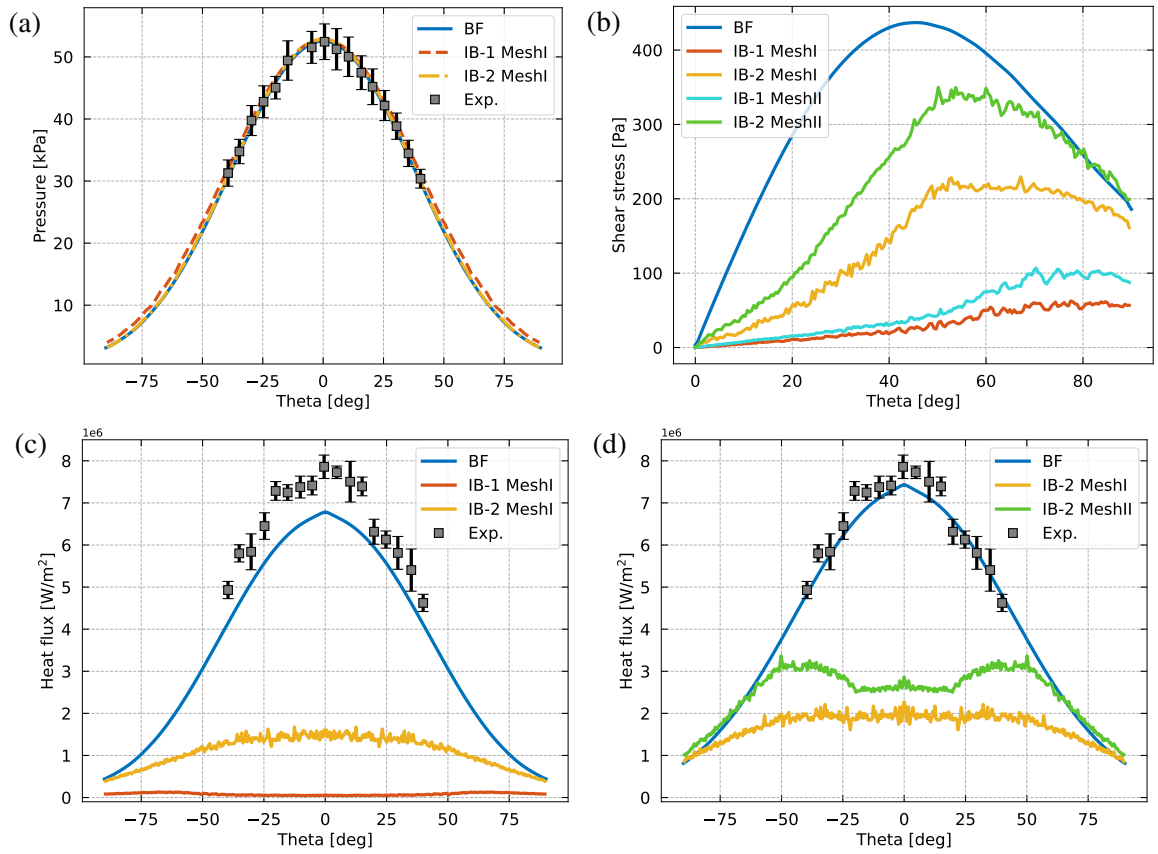

Figure 8: Pressure (a), shear stress (b) and heat flux for non-catalytic (c) and catalytic (d) wall for the *Knight* test.

4.3 Subsonic reactive flow past an ablative sample

This test case is a simplification of an experimental campaign conducted in the Plasmatron facility at the von Karman Institute [27] to determine the massblowing rate for a nitrogen subsonic flow around an axis-symmetric hemispherical sample ($r = 0.025\,m$).

The flow conditions selected are referred to as *G*7 in [27]. Nevertheless, since the goal of the present test case is a code-to-code verification, two main simplifications were adopted to reduce the computational cost [29]: the geometry of the sample is planar and electrons are neglected in the mixture (N_2, N, C_3,

C_2, C, CN). Free stream conditions are reported in table 3. The wall is considered isothermal and non-catalytic. Nitridation boundary condition is imposed following the formulation found by Helber et al. [27], shown in Eq. (17).

Table 3: Free stream conditions for the ablative test case.

u_∞ [m/s]	Re_∞	T_∞ [K]	T_w [K]	p_∞ [Pa]	Y_{N_2}	Y_N
1570	36.7	10280	2407	1500	9.77659e-05	0.9999022341

The computational domain considered extends for $25r$ to avoid wave reflections from the boundaries. Wall resolution of the BF grid has been imposed after the grid independence study (see Appendix A) to $\Delta n_w = 1 \times 10^{-5}$ m. IB mesh presents a similar resolution ($\Delta n_w = 7 \times 10^{-6}$ m). Stagnation line profiles are shown in Fig. 9. A very good agreement with BF results is observed for both IB methods. Wall quantity profiles are shown in Fig. 10.

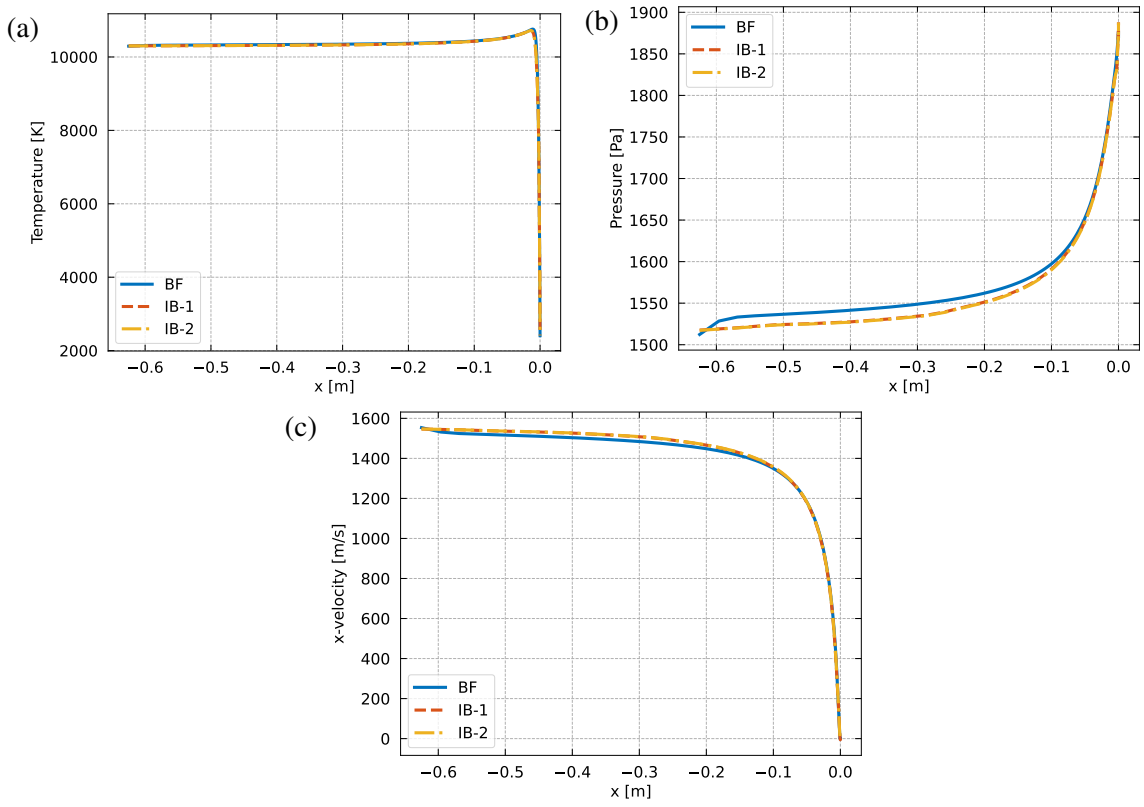

Figure 9: Stagnation line profile for the ablation test case: gas temperature (a), pressure (b) and axial velocity (c).

5. Conclusions

This work presents numerical results for high-temperature flows in the context of hypersonic entry applications, using different numerical strategies, namely a *body-fitted* approach used as reference, and two different *immersed-boundary* techniques. Numerical investigations highlight how a linear reconstruction of the solution in the thermal boundary layer is not suitable for isothermal wall boundary condition, which provokes a sharp temperature gradient. On the contrary, the ghost-cell method proposed solves such an issue. The adiabatic wall simulation confirms that the most critical issue is the reconstruction of the temperature. Indeed, as soon as the temperature gradient is null, the shock stand-off distance is in a perfect agreement between the three methods employed.

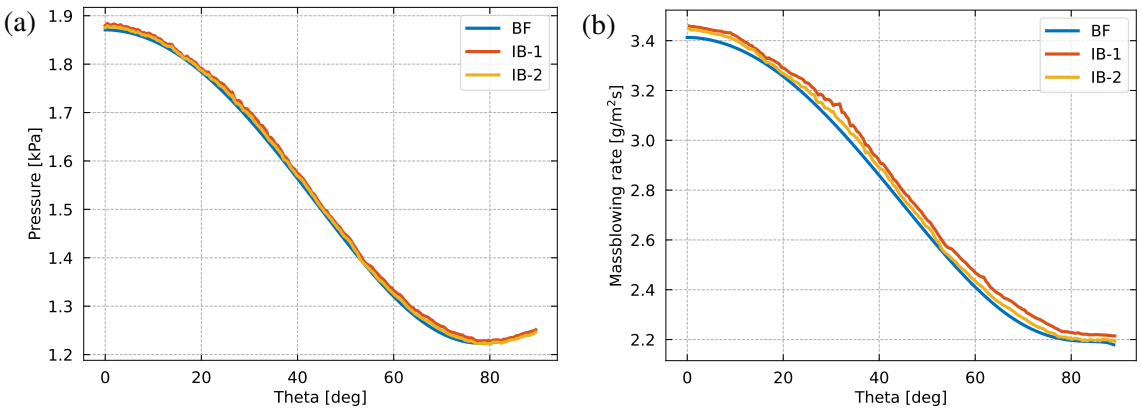

Figure 10: Pressure (a) and massblowing rate (b) for the ablation test.

A. Body-fitted mesh independence studies

Mesh independence studies have been conducted on BF grids to estimate the wall resolution which provides grid converged results for each test case. For all the test cases, the number of nodes has been doubled-up in order to obtain geometrically similar grids [30].

Specifically, two different grids have been constructed for the *M3C* test, as reported in table A.1. Wall quantity profiles are reported in Fig. A.1. From this analysis, IB meshes have been constructed by imposing a wall resolution of $\Delta n_w = 1 \times 10^{-5}$ m.

Table A.1: Computational grids employed for the *M3C* test.

Refinement level	Grid cells	Shock resolution [m]	Wall resolution [m]
Mesh I	100×50	2×10^{-5}	2×10^{-5}
Mesh II	200×100	1×10^{-5}	1×10^{-5}

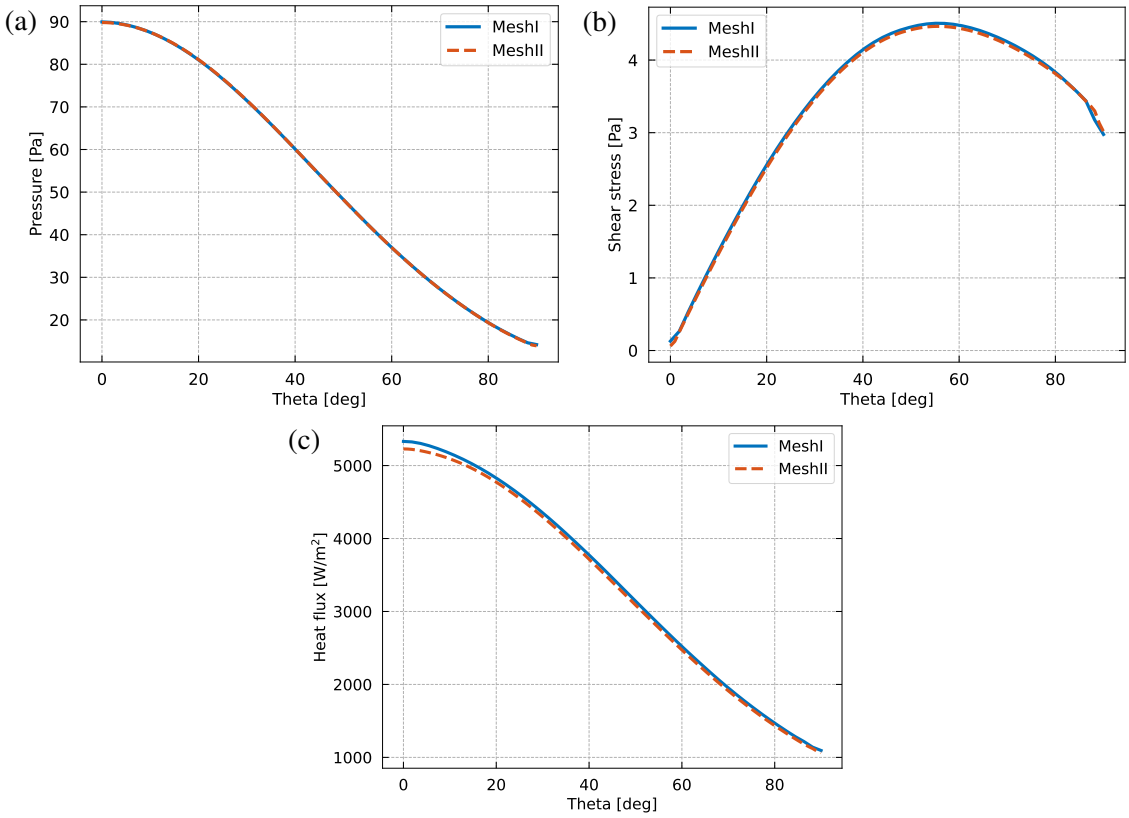

Figure A.1: Wall quantity profiles for two different grids for the *M3C* test: pressure (a), shear stress (b) and heat flux (c).

For the *Knight* test case, a wider investigation was necessary because of the sharper wall gradients. More in detail, four different computational grids ahve been used for the grid independence analysis. All their details are reported in table A.2. It is mandatory to specify the this study was conducted only for the inert wall case, assuming that catalysis does not influence the numerical convergence of the solution. Wall quantity profiles are reported in Fig. A.2. From this analysis, MeshIII has been selected for further investigation on both BF and IB simulations.

Lastly, grid convergence is shown for the ablation test case. Dealing with a subsonic flow, numerical results converge quite easily on relatively coarse grids. Hence, only two refinement levels have been investigated: these are reported in table A.3, whereas wall quantity profiles are shown in Fig. A.3. For

Table A.2: Computational grids employed for the *Knight* test [28].

Refinement level	Grid cells	Shock resolution [m]	Wall resolution [m]
MeshI	100×50	1×10^{-5}	2×10^{-7}
MeshII	200×100	5×10^{-6}	1×10^{-7}
MeshIII	400×200	2.5×10^{-6}	5×10^{-8}
MeshIV	800×400	1.25×10^{-6}	2.5×10^{-8}

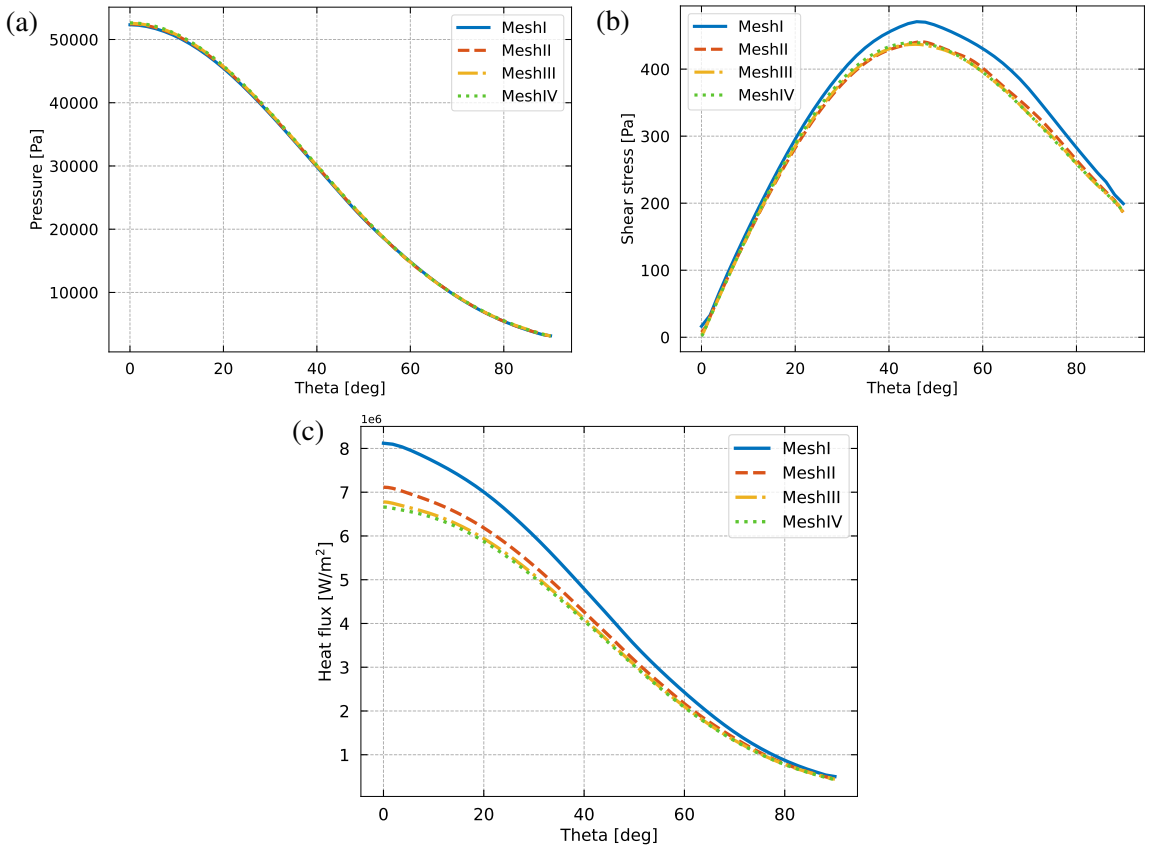

Figure A.2: Wall quantity profiles for two different grids for the *Knight* test: pressure (a), shear stress (b) and heat flux (c).

this test, MeshI already provides grid independent results.

Table A.3: Computational grids employed for the ablation test.

Refinement level	Grid cells	Wall resolution [m]
MeshI	100×60	1×10^{-5}
MeshII	200×120	5×10^{-6}

Acknowledgements

D. Ninni, F. Bonelli and G. Pascazio were partially supported by the Italian Ministry of Education, University and Research under the Program Department of Excellence Legge 232/2016 (Grant No. CUP - D93C23000100001).

F. Bonelli was funded by the European Union – Next Generation EU – Piano Nazionale Resistenza e

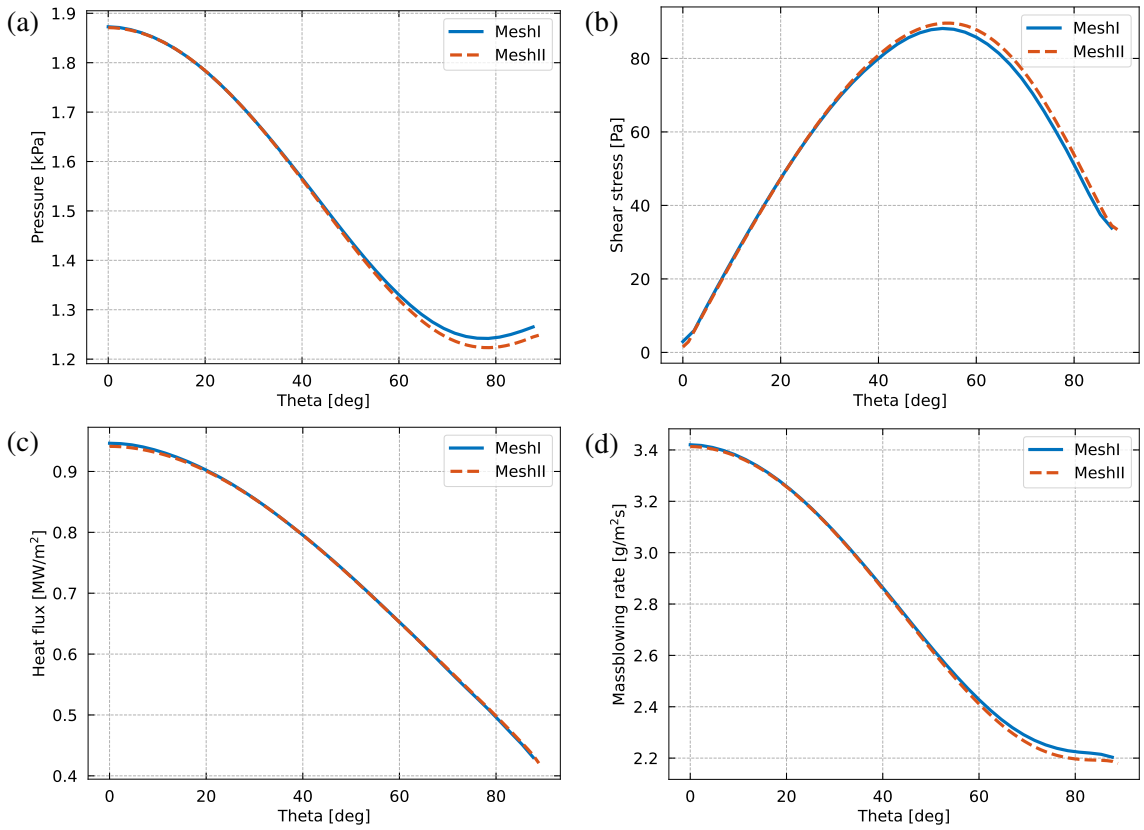

Figure A.3: Wall quantity profiles for two different grids for the ablation test: pressure (a), shear stress (b), heat flux (c) and massblowing rate (d).

Resilienza (PNRR), Missione 4 Componente C2 Investimento 1.1 – Decreto Direttoriale n. 1409 del 14/09/2022, Bando PRIN 2022 PNRR, CUP D53D23018520001.

The authors acknowledge the CINECA award under the ISCRA initiative, for the availability of high performance computing resources and support under the allocation HP10CT0KPU.

This study was carried out within the Space It Up and received funding from the ASI and the MUR – Contract n. 2024-5-E.0- CUP n. I53D24000060005.

References

[1] Graham V Candler. Rate effects in hypersonic flows. *Annual Review of Fluid Mechanics*, 51:379–402, 2019.

[2] Davide Ninni. Development of a multi-GPU solver for atmospheric entry flows with gas-surface interactions. *PhD Thesis*, 2022.

[3] Nagi N Mansour, Francesco Panerai, Jean Lachaud, and Thierry Magin. Flow mechanics in ablative thermal protection systems. *Annual Review of Fluid Mechanics*, 56(1):549–575, 2024.

[4] Graham V Candler, Heath B Johnson, Ioannis Nompelis, Vladimyr M Gidzak, Pramod K Subbareddy, and Michael Barnhardt. Development of the US3D code for advanced compressible and reacting flow simulations. In *53rd AIAA Aerospace Sciences Meeting*, page 1893, 2015.

[5] Thomas D Economon, Francisco Palacios, Sean R Copeland, Trent W Lukaczyk, and Juan J Alonso. SU2: An open-source suite for multiphysics simulation and design. *Aiaa Journal*, 54(3):828–846, 2016.

[6] Rajat Mittal and Gianluca Iaccarino. Immersed boundary methods. *Annu. Rev. Fluid Mech.*, 37:239–261, 2005.

[7] Somnath Roy, Ashoke De, and Elias Balaras. Immersed Boundary Method. 2020.

[8] Giuseppe Pascazio, Davide Ninni, Francesco Bonelli, and Gianpiero Colonna. Hypersonic flows with detailed state-to-state kinetics using a GPU cluster. In *Plasma Modeling (Second Edition): Methods and applications*. IOP Publishing, 2022.

[9] Kenneth Kuan-yun Kuo and Ragini Acharya. *Fundamentals of turbulent and multiphase combustion*. John Wiley & Sons, 2012.

[10] CR Wilke. A viscosity equation for gas mixtures. *The journal of chemical physics*, 18(4):517–519, 1950.

[11] EA Mason and SC Saxena. Approximate formula for the thermal conductivity of gas mixtures. *The Physics of fluids*, 1(5):361–369, 1958.

[12] GSR Sarma. Physico–chemical modelling in hypersonic flow simulation. *Progress in Aerospace Sciences*, 36(3-4):281–349, 2000.

[13] R Byron Bird, Warren E Stewart, and Edwin N Lightfoot. *Transport Phenomena revised 2nd Edition*. John Wiley & Sons, Inc New York, 2006.

[14] Joseph O Hirschfelder, Charles F Curtiss, and R Byron Bird. *The molecular theory of gases and liquids*. John Wiley & Sons, 1964.

[15] Joseph L Steger and RF Warming. Flux vector splitting of the inviscid gasdynamic equations with application to finite-difference methods. *Journal of computational physics*, 40(2):263–293, 1981.

[16] Bram Van Leer. Towards the ultimate conservative difference scheme. V. A second-order sequel to Godunov's method. *Journal of computational Physics*, 32(1):101–136, 1979.

[17] Guang-Shan Jiang and Chi-Wang Shu. Efficient implementation of weighted ENO schemes. *Journal of computational physics*, 126(1):202–228, 1996.

[18] Jan G Verwer. Gauss–Seidel iteration for stiff ODEs from chemical kinetics. *SIAM Journal on Scientific Computing*, 15(5):1243–1250, 1994.

[19] Elias Balaras. Modeling complex boundaries using an external force field on fixed Cartesian grids in large-eddy simulations. *Computers & Fluids*, 33(3):375–404, 2004.

[20] EA Fadlun, Roberto Verzicco, Paolo Orlandi, and J Mohd-Yusof. Combined immersed-boundary finite-difference methods for three-dimensional complex flow simulations. *Journal of computational physics*, 161(1):35–60, 2000.

[21] Chul Park. *Nonequilibrium hypersonic aerothermodynamics*. John Wiley & Sons, 1989.

[22] Chul Park. Review of chemical-kinetic problems of future NASA missions. I-Earth entries. *Journal of Thermophysics and Heat transfer*, 7(3):385–398, 1993.

[23] Chul Park, John T Howe, Richard L Jaffe, and Graham V Candler. Review of chemical-kinetic problems of future NASA missions. II-Mars entries. *Journal of Thermophysics and Heat transfer*, 8(1):9–23, 1994.

[24] Graham V Candler and Robert W MacCormack. Computation of weakly ionized hypersonic flows in thermochemical nonequilibrium. *Journal of Thermophysics and heat transfer*, 5(3):266–273, 1991.

[25] Roger C Millikan and Donald R White. Systematics of vibrational relaxation. *The Journal of chemical physics*, 39(12):3209–3213, 1963.

[26] Paolo Francesco Barbante. *Accurate and efficient modelling of high temperature nonequilibrium air flows*. PhD thesis, 2001.

[27] Bernd Helber, Alessandro Turchi, and Thierry E Magin. Determination of active nitridation reaction efficiency of graphite in inductively coupled plasma flows. *Carbon*, 125:582–594, 2017.

[28] Doyle Knight, José Longo, Dimitris Drikakis, Datta Gaitonde, Andrea Lani, Ioannis Nompelis, Bodo Reimann, and Louis Walpot. Assessment of CFD capability for prediction of hypersonic shock interactions. *Progress in Aerospace Sciences*, 48:8–26, 2012.

[29] Ata O Baskaya, Michele Capriati, Davide Ninni, Francesco Bonelli, Giuseppe Pascazio, Alessandro Turchi, Thierry Magin, and Stefan Hickel. Verification and Validation of Immersed Boundary Solvers for Hypersonic Flows with Gas-Surface Interactions. In *AIAA AVIATION 2022 Forum*, page 3276, 2022.

[30] Tyrone S Phillips and Christopher J Roy. Richardson extrapolation-based discretization uncertainty estimation for computational fluid dynamics. *Journal of Fluids Engineering*, 136(12), 2014.